PCCP



PAPER View Article Online



Cite this: Phys. Chem. Chem. Phys., 2018, 20, 19515

Theoretical evidence of low-threshold amplified spontaneous emission in organic emitters: transition density and intramolecular vibrational mode analysis

Lin Ma, (1)†a Yue Yu, (10)†*a Bo Jiao, b Xun Houb and Zhaoxin Wu (10)*bc

Organic gain materials are highly attractive for lasing due to their chemical tunability and large stimulated emission cross sections. In previous reports, the radiative decay rate k_r was considered as an important factor to determine outstanding amplified spontaneous emission (ASE) performance of organic molecules. In this study, we use quantum mechanics to reveal the influential factors on photophysical properties of organic emitters, and give insight into the effect of k_r on ASE performance. Based on the theoretical analysis of three molecules with similar structure, calculated results show that large k_r derives from enhanced transition density ρ between the electronic wave functions of the ground-state and the lowest excited singlet state as well as a handful of low-frequency torsional modes with small Huang–Rhys factor S, further, k_r values are calculated depending on molecular vibration terms. In addition, through the analysis of non-radiative decay rate k_{nr} considering vibration terms (vibronic coupling constants), the comparison of k_r and k_{nr} shows that the radiative decay process is promoted in the three molecules. The two aspects are desired for outstanding ASE performance. Our work shows that the roles of transition density and vibrational modes are crucial to clarify the photophysical properties, which govern the ASE performance in organic light emitters.

Received 5th March 2018, Accepted 29th June 2018

DOI: 10.1039/c8cp01448e

rsc.li/pccp

1 Introduction

Efficient organic luminescent materials have attracted great attention due to their potential applications in organic solid-state lasing in recent years. Amany organic semiconductor molecules demonstrate amplified spontaneous emission (ASE) on account of their superior photophysical properties and wide tunable laser wavelength. Besides, they have become very attractive materials for a range of photonic devices including light-emitting diodes, photovoltaic cells and organic field effect transistors. On their superior photophysical properties and wide tunable laser wavelength.

In general, it was reported that the factors of the Stokes shift, the radiative decay rate $(k_{\rm r})$, the non-radiative decay rate $(k_{\rm nr})$, the fluorescence lifetime $(\tau_{\rm r})$ and the fluorescence quantum yield (Φ) are correlated with the stimulated emission phenomenon. Adachi and co-authors proposed that the

Fax: +86-29-82664867; Tel: +86-29-82664867

radiative decay rate k_r is intrinsic to the nature of ASE performance. In their work, they investigated the photophysical properties of a series of molecules with similar molecular structures, 15 and found that a larger $k_{\rm r}$ corresponding to high quantum efficiency Φ and short fluorescence lifetime τ_r resulted in outstanding ASE performance. Then, a series of low ASE threshold materials were reported with high k_r ($k_r = \Phi/\tau_r$). ¹⁶⁻²¹ Among the reported molecules, octafluorene possesses the lowest ASE threshold (90 nJ cm⁻²) with the largest k_r (1.7 × 10⁹ s⁻¹).²¹ Different molecular configurations have distinct k_r , thus, the molecular structures have a straightforward influence on excited-state radiative processes and a few studies researched excited-state decay processes based on organic luminescent molecules. 22-24 In our previous work, we provided the relationship between the molecular conformation and a four-level system to understand the ASE characteristics. 25,26 However, it is hard to understand the intrinsic factors determining k_r for ASE characteristics in view of the energy level system. In order to explicate the effect of molecular structure on photophysical properties $(k_r \text{ and } k_{nr})$ for ASE performance, it is important to investigate the excited-state properties in organic semiconductor materials. In this respect, the analytical vibration correlation function approach should be employed for understanding the ASE characteristics for organic semiconductor molecules.

^a School of Physics and Optoelectronic Engineering, Xidian University, Xi'an 710071, P. R. China. E-mail: yyu@xidian.edu.cn; Tel: +86-29-88202554

b Key Laboratory of Photonics Technology for Information, School of Electronic and Information Engineering, Xi'an Jiaotong University, Xi'an 710049, P. R. China

^c Collaborative Innovation Center of Extreme Optics, Shanxi University, Taiyuan 030006, China. E-mail: zhaoxinwu@mail.xjtu.edu.cn;

[†] These authors contributed equally to this work.

Well-defined chemical systems help to better understand laser material requirements to promote the development of optical gain molecules.

As already proved, the ASE threshold $E_{\rm th}$ is expressed by the equation: $E_{\rm th} \propto 1 + k_{\rm nr}/k_{\rm r}$, where $k_{\rm r}$ and $k_{\rm nr}$ are the radiative decay rate and the non-radiative decay rate, respectively.²⁷ We can see that E_{th} is inversely proportional to k_{r} , further, k_{r} and k_{nr} both have influence on $E_{\rm th}$. In order to research the influential factors for ASE performance, we need to have an insight into the intrinsic factors of molecular structure for photophysical properties. In this paper, for typical organic light emitters N,N'diphenyl-N,N'-bis(3-methylphenyl)-(1,1'-biphenyl)-4,4'-diamine (TPD), 4,4'-bis(3-mehtylcarbazol-9-vl)-2,2'-biphenyl (mCBP) and N,N'-diphenyl-N,N'-bis(1-naphthyl)-1,1'-biphenyl-4,4"-diamine (NPB), we investigate the molecular geometries, electron density, and vibrational modes to reveal the relationship between molecular conformation and photophysical properties. Then, we can further understand the intrinsic factors governing ASE performance in organic emitters. Through theoretical analysis, $k_{\rm r}$ of the excited-state decay processes for TPD, mCBP and NPB are calculated under the adiabatic approximation in consideration of molecular vibration terms. Visualization of transition density distribution ρ , Huang-Rhys factors S and vibronic coupling constants provide a physical insight into the photophysical properties of optical gain emitters. Our calculation results demonstrate that enhanced transition density and a handful of low-frequency torsional modes lead to large k_r . Besides, k_{nr} for given molecules are comparable. k_r is an order of magnitude smaller than $k_{\rm nr}$ for NPB, thus, non-radiative decay plays a leading role in NPB compared with that in TPD and mCBP. As we know, high luminescence efficiency of organic light emitters requires a faster rate of $S_1 \rightarrow S_0$ radiative decay than that of competitive $S_1 \rightarrow S_0$ nonradiative decay, which is benefit for ASE performance. Our work provides theoretical evidence to reveal the influential factors for photophysical properties, and further explains the effect of k_r on ASE performance.

2 Methodology

 $k_{\rm r}$ and $k_{\rm nr}$ are important parameters for excited-state decay processes. Under the assumed adiabatic approximation of different time scales for electronic and nuclear motion, the vibronic part of the total wave function contributes only through Franck-Condon overlap factors. Restricting the discussion to the lowest vibronic level, $|0_{\rm e}\rangle$, of the first excited-state vibronic level as the initial state, the probability to emit through a transition to the $n_{\rm th}$ vibrational level of the ground-state, $|n_{\rm g}\rangle$, is given by Fermi's golden rule:²⁹

$$P(|0_{e}\rangle \to |n_{g}\rangle) = \frac{2\pi}{\hbar} |E \cdot \mu|^{2} |\langle 0_{e} | n_{g}\rangle|^{2}$$

$$\times \delta(E_{L} + E_{\text{HOMO}} - E_{\text{LUMO}} - n_{g}\hbar\omega)$$
(1)

where E is the external electric field at energy $E_{\rm L}$, μ is the electric transition dipole moment, and $\hbar\omega$ is the effective

vibrational mode. The Franck–Condon factor can be expressed by a Poisson distribution with the Huang–Rhys factor, *S*:

$$\left|\left\langle 0_{\rm e} \mid n_{\rm g} \right\rangle \right|^2 = \frac{S^n}{n!} {\rm e}^{-S} \tag{2}$$

In the Poisson distribution over the vibronic levels, S_j is the Huang–Rhys factor which characterizes the modification of vibrational quanta (absorbed or emitted) when going from one electronic state to another:

$$S_{j} = \frac{\omega_{j} (\Delta Q_{j})^{2}}{2\hbar} \tag{3}$$

where ΔQ_j represents the displacement along the normal mode (NM)_j between the equilibrium positions of the two electronic states, and ω_j is the harmonic vibrational frequency for the *j*th vibrational mode.

The reorganization energy λ_j on the potential energy surface (PES) of the electronic ground-state is expressed in terms of the Huang–Rhys factor S_i of the mode:

$$\lambda_i = S_i \hbar \omega_i \tag{4}$$

From the above, here, we consider a system consisting of a collection of harmonic oscillators without considering the Duschinsky rotation effect (mode mixings), and the radiative decay rate is obtained:²²

$$k_{\rm f(i0\to f)} = \frac{64\pi^4}{h^4 c^3} |\mu|^2 N_{\rm FC}$$
 (5)

$$N_{\rm FC} = \sum_{n} \left(E_{\rm if} + \sum_{j} n_j \hbar \omega_j \right)^3 \prod_{j} \frac{S_j^{n_j}}{n_j!} e^{-S_j} \tag{6}$$

where \hbar is the Planck constant, c is the speed of light in vacuum, E_{if} is the transition energy from the initial state (usually S_1) to the final state (usually S_0), and μ is the electric transition dipole moment between the two states.

Besides, $k_{\rm nr}$ also depends on vibrational terms resulting from vibrational wavefunctions. To confirm this point, we also calculated the vibronic coupling constant, V_j , which is related to the reorganization energy, λ_j . V_j measures the strength of intramolecular vibronic coupling caused by the jth intramolecular vibrational mode: 31,32

$$V_i^2 = 2\omega_i^2 \lambda_i \tag{7}$$

$$k_{\rm nr} = 2\pi \sum_{i} P_j (V_j)^2 / E_{\rm if}^2$$
 (8)

where P_i denotes the vibrational terms and can be written as:

$$P_{j} = \frac{\sum_{n} (n+1/2) \exp\left\{-(n+1/2)\omega_{j}/k_{\mathrm{B}}T\right\}}{\sum_{n} \exp\left(-\omega_{j}/k_{\mathrm{B}}T\right)}$$
(9)

where E is the $S_1 \leftarrow S_0$ excitation energy, and n denotes the vibrational state.

The molecular equilibrium geometries of TPD, mCBP and NPB in the S_0 states were optimized at the density functional theory (DFT) level using the B3LYP functional with the

6-31G basis set. We used time-dependent density functional theory (TD-DFT) for the calculation of the S1 states with the same functional and basis set. The oscillator strengths, dipole moments and vertical excitation energies were obtained with TDDFT based on the S₁ optimized geometries. Here, we mainly focused on radiative and non-radiative decay processes, thus, based on the molecules in the So optimized geometries, the vibrational frequency (ω_i) for each normal mode was calculated using the DUSHIN program developed by Weber, Cai, and Reimers.³³ Then, the Huang-Rhys factors (S_i) were calculated depending on the geometric change between the So states and S₁ states. Likewise, the reorganization energies were calculated in the S₀ states. All the calculations were performed using the Gaussian 09 D01 program package. We further used the Multiwfn software 3.3.9 version to calculate the transition density matrices using the S₁ optimized geometries.

3 Results and discussion

Photophysical properties

Fig. 1 presents the chemical structures of TPD, mCBP and NPB. Table 1 gives the photophysical properties and ASE characteristics from experiment of the three compounds based on solid films (100 nm).¹⁵ As reported, the pumping power threshold for ASE (E_{th}) was found by measuring the spectral change of photoluminescence (PL), using a N2 gas laser as an excitation source in an optical chamber with N₂ flowing. By increasing the excitation power further, the PL intensity abruptly increased and clear E_{th} was observed, and the full width at half maximum (FWHM) of the emission spectrum was dramatically reduced at the threshold. In experiment, TPD and mCBP demonstrate typical optical gain properties with low ASE thresholds E_{th} , while, NPB shows no ASE. 15 In addition, we find that TPD possesses identical $E_{\rm th}$ to mCBP but larger $\Delta G_{\rm ASE}$ (the slope being the ratio of the output ASE power divided by the excitation power). Accordingly, TPD with the highest ASE gain has the highest radiative decay rate, $k_r = 6.8 \times 10^8 \text{ s}^{-1}$. For mCBP with terminal carbazole groups, a rather low ASE gain corresponds to an intermediate value of $k_{\rm r}$ (3.5 \times 10⁸ s⁻¹), while, NPB shows the lowest value ($k_r = 0.8 \times 10^8 \text{ s}^{-1}$) when the terminal group is replaced with naphthyl. As well, according to equation $\Phi = k_{\rm r}/(k_{\rm r} + k_{\rm nr})$, $k_{\rm nr}$ for the three molecules are comparable, calculated as below: $k_{\rm nr}$ is 9.7 \times 10⁸ s⁻¹ for TPD, 3.6 \times 10⁸ s⁻¹ for mCBP, and 2.1 \times 10⁸ s⁻¹ for NPB. As a result, k_r is one decade smaller compared with $k_{\rm nr}$ for NPB, which is different from TPD and mCBP.

Table 1 Experimental values for photophysical properties and ASE characteristics of TPD, mCBP and NPB based on solid films (100 nm) in ref. 15

Compound	$\lambda_{\mathbf{f}}^{\ a}$	$k_{\rm r}^{\ b} \left(10^8 \ {\rm s}^{-1}\right)$	$E_{\rm th}^{c} \left(\mu \mathrm{J \ cm}^{-2} \right)$	$\Delta G_{\mathrm{ASE}}{}^d$	FWHM ^e (nm)
TPD	424	6.8	1.8	12	3.4
mCBP	400	3.5	1.7	4	4.1
NPB	445	0.8	_	_	_

^a Fluorescence peak wavelength. ^b Radiative decay rate. ^c Excitation power threshold for ASE. ^d ASE gain. ^e Full width at half maximum (FWHM) of the ASE spectrum.

Shown as the parameters above, we can summarize that the absence of ASE in NPB originates from low k_r . The results are indicative of the fact that k_r , controlling the ASE threshold, strongly depends on the molecular structure, which has to be fully understood. Hence, theoretical elucidation needs to be applied to analyze the intrinsic factors determining the radiative decay rate, furthermore, calculated k_r is required as well.

3.2 Geometric and electronic structures

In order to obtain the molecular geometries, the optimized molecular geometries of the ground-states and first excited-states with similar dipole moments (0.1289 D and 0.1048 D for TPD, 0.3388 D and 0.3584 D for mCBP, and 1.5513 D and 1.5292 D for NPB) were calculated, which prove the accuracy of the optimized geometries. The three molecules possess a common central biphenyl core and different peripheral substituents. The optimized equilibrium geometries at the ground-states So and the first excited-states S₁ are given in Table 2. Twisted structures for the three molecules are obtained. By analyzing the structural changes, $|\Delta(S_0 - S_1)|$, we can see that the modifications mainly derive from the twisted dihedral angles between the central biphenyl core and peripheral groups upon excitation. The change of torsional angles in mCBP is larger than that in TPD, because the carbazole unit is planar and bulkier than the phenyl substituent. Especially for NPB, we observe the most significant modification of dihedral angles with 61.1° and 57.1°, which is mainly because naphthyl produces a weak rotation potential. The remarkable structural changes signify large geometry relaxations (large reorganization energies λ) following excitation, corresponding to dominant non-radiative decay processes relative to radiative decay processes. Then, the non-radiative decay processes directly compete with the radiative decay processes, which negatively affects the ASE performance. This will be discussed in more detail below.

The molecular geometries validly affect the electronic density distributions, presented in Fig. 2. Electron density contours



Fig. 1 Chemical structure of TPD, mCBP and NPB.

Table 2 Selected bond lengths (Å) and dihedral angles (deg) of optimized geometries for TPD, mCBP and NPB

	TPD			mCBP	mCBP			NPB		
	S_0^a	$S_1^{\ b}$	$\left \Delta(S_0-S_1)\right ^c$	S_0^a	$S_1^{\ b}$	$\left \Delta(S_0-S_1)\right ^c$	S_0^a	$S_1^{\ b}$	$ \Delta(S_0 - S_1) ^c$	
$R_{\rm C}$	1.482	1.440	0.042	1.483	1.439	0.044	1.480	1.449	0.031	
L	1.420	1.430	0.010	1.419	1.448	0.029	1.420	1.393	0.027	
α	35.6	10.6	25.0	37.2	9.3	27.9	35.3	19.5	15.8	
β	40.4	53.4	13.0	54.5	89.5	35.0	44.4	-17.2	61.6	
γ	41.1	53.5	12.4	_	_	_	32.8	-24.2	57.0	

^a Optimized geometries in the ground-state. ^b Optimized geometries in the first excited-state. ^c Structural changes between the two states.

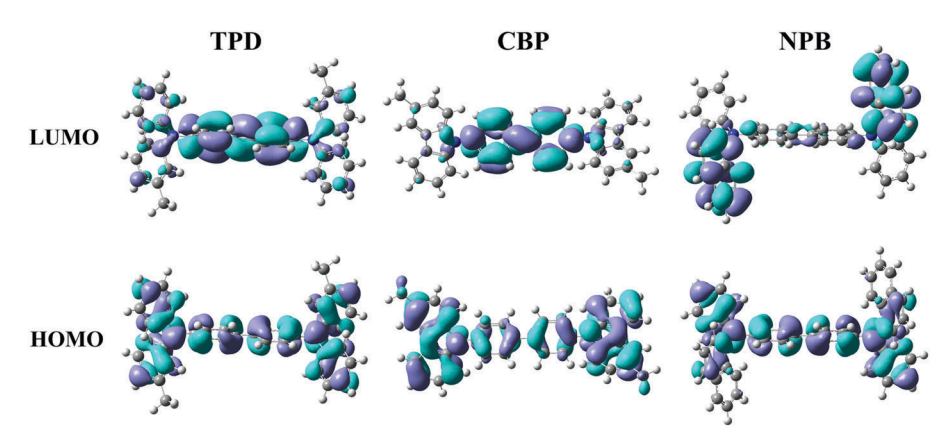


Fig. 2 Calculated spatial distributions of HOMO and LUMO levels for TPD, mCBP and NPB. The isosurface value for the HOMOs and the LUMOs is 0.02 atomic units (purple regions: positive; blue regions: negative).

Table 3 Photophysical parameters obtained by TD-DFT/B3LYP/6-31G(d,p) based on optimized geometries

	E^{a} (eV)					
Compound	Absorption	Emission	Transition	Contribution (%)	μ^b (a.u.)	$k_{\rm r}^{\ c} (10^8 \ { m s}^{-1})$
TPD	3.40	2.89	HOMO-LUMO	98.16	4.114	5.53
mCBP NPB	3.50 3.59	2.98 2.78	HOMO-LUMO HOMO-LUMO	98.83 96.51	3.518 0.817	3.15 0.47
1112	0.03	2.70	HOMO-1-LUMO	3.09	0.017	0.17

^a Vertical transition energies. ^b Electric transition dipole moments. ^c Theoretical radiative decay rates.

of HOMOs and LUMOs were calculated based on DFT. HOMO-LUMO excitation predominantly contributes to S₁ in all cases (see Table 3): the HOMO and LUMO distributions have significant effects on the luminescence efficiencies of these materials. For TPD, the HOMO is localized in the whole molecular skeleton, and the LUMO is mainly localized in the biphenyl core and spreads less over the peripheral phenyl groups because of the lengthened π -conjugation of biphenyl compared with that of phenyl. For mCBP, the HOMO is localized in the whole molecular skeleton, and the LUMO is localized in the biphenvl core due to the electron-donating nature of carbazole. Interestingly, NPB exhibited considerable change, there is a greater spatial separation of the HOMO and LUMO wavefunction densities. The bulky naphthyl groups have enhanced conjugation compared with the biphenyl group and demonstrate electronwithdrawing character to some extent. Thus, the LUMO spreads over the peripheral naphthyl groups instead of the biphenyl core. Therefore, the HOMO-LUMO overlap is larger for TPD and

mCBP than for NPB and the behavior of the two naphthyl groups is expected to dominate the photophysical properties. In general, small overlap between the HOMO and LUMO will result in small $k_{\rm r}$ which is agreement with the experimental results.

3.3 Transition energies and transition dipole moments

Based on the optimized geometries, we undertook TDDFT calculations to further research the optical properties of TPD, mCBP and NPB. The calculated electric transition dipole moments (μ) and vertical excitation energies (E) are given in Table 3. According to eqn (5), $k_{\rm r}$ is proportional to $|\mu|^2$, where μ is a three-dimensional vector called the transition dipole moment for the electron transition, and μ can be expressed in terms of ρ as:³⁰

$$\boldsymbol{\mu} = \int \rho(\mathbf{x})(-e\mathbf{x}) d\mathbf{x} \tag{10}$$

where ρ is the transition density for the S_1 state and x denotes a point in three-dimensional space. The coordinate origin is set

PCCP

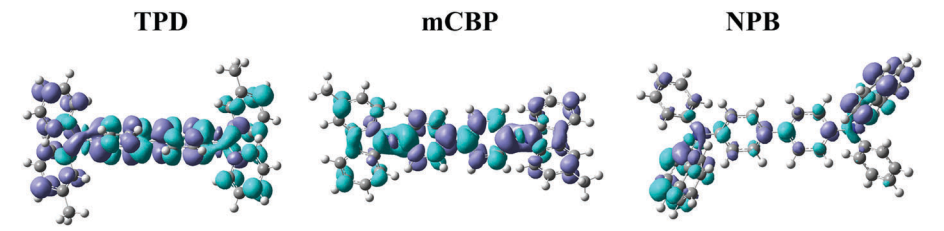


Fig. 3 Transition densities ρ associated with the S₁ \leftarrow S₀ excitation of TPD, mCBP and NPB. The isosurface value for ρ is 0.0004 atomic units (purple regions: positive; blue regions: negative)

as the center of the atomic charge. From the equation above, the elements of μ become large when ρ has a value at x at which these elements are large, *i.e.*, when ρ is distributed in regions that are distant from the coordinate origin. Fig. 3 presents the transition densities for the researched molecules. Because the HOMO-LUMO overlap is larger for TPD and mCBP than for NPB, ρ is thus more widely distributed for TPD and mCBP. Thus, ρ spreads over the central biphenyl core and extends over peripheral substituents that are distant from the coordinate origin for TPD and mCBP. Because of this wide ρ distribution, TPD has a sizable μ of 4.114 atomic units and mCBP has a comparable μ of 3.518 atomic units. In contrast, NPB has a small μ of 0.817 atomic units because the ρ distribution range is limited to small regions located on naphthyl groups. This is because the LUMO of NPB is distributed on naphthyl groups (Fig. 2) and the resulting HOMO-LUMO overlap is thus small.

Interestingly, simple replacement with naphthyl units in NPB causes μ to decrease markedly, and the $S_1 \rightarrow S_0$ radiative decay is thus significantly suppressed. To investigate the effect of this chemical modification on μ further, according to eqn (10), we introduce a three-dimensional function called the transition dipole moment density τ :³⁰

$$\tau(\mathbf{x}) = \rho(\mathbf{x})(-e\mathbf{x}) \cdot \frac{\mu}{|\mu|} \tag{11}$$

 μ can then be expressed as:

$$\mu = \int \tau(\mathbf{x}) d\mathbf{x} \tag{12}$$

We can capture the features of μvia transition dipole moment density analysis. By visualizing the τ distributions of the three molecules, we can obtain physical insights into the relationships between the molecular structures and μ values. Fig. 4 shows the τ distributions and fragment μ for TPD, mCBP and NPB. Through comparison of the τ distributions, we find that τ distributes much more widely for TPD and mCBP than for NPB.

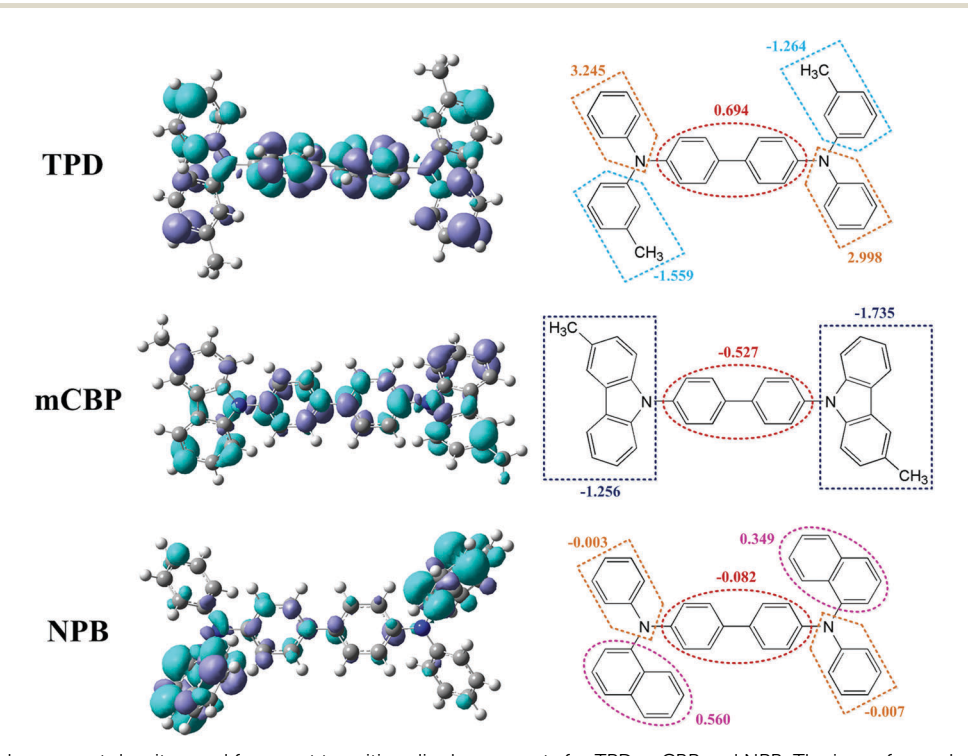


Fig. 4 Transition dipole moment density τ and fragment transition dipole moments for TPD, mCBP and NPB. The isosurface value for τ is 0.001 atomic units (purple regions: positive; blue regions: negative). The numbers indicate the fragment transition dipole moments in atomic units. The sum of these fragment transition dipole moments gives the magnitude of the transition dipole moment μ

Paper

Therefore, the spatial integrals of τ for TPD and mCBP are larger than that of NPB, which enhances the transition dipole moment μ . As well, Fig. 4 presents the spatial integrals of τ that were calculated for the fragment structures and the sum of these fragment transition dipole moments is equal to the total μ value. For NPB, the major contribution to μ originates from naphthyl groups. However, the fragment transition dipole moments of the fragments for TPD and mCBP are approximately ten times those for NPB. This leads to μ of TPD and mCBP (4.114 and 3.518 atomic units) being larger than that of NPB (0.817 atomic units).

According to the discussion above, we conclude that the weak transition dipole moment for NPB with naphthyl moieties derives from the small HOMO–LUMO overlap, small ρ and small τ (see Fig. 2 to Fig. 4). Moreover, the weak electronic transition would be expected to result in a small radiative decay rate $k_{\rm r}$ according to eqn (5). A large transition dipole moment, namely the strength of the electronic transition, enhances the radiative decay process. TPD and mCBP possess strong electronic transitions compared to NPB, which benefits ASE performance. More detailed research is required to reveal the influential factors for the radiative decay rate considering eqn (6) with vibrational terms, which governs ASE performance.

3.4 Vibrational modes and Huang-Rhys factors

According to eqn (5)–(8), k_r and k_{nr} should be analyzed with vibrational terms. The vibrational modes of TPD, mCBP and

NPB were obtained based on the optimized molecular geometries. The Huang-Rhys factor, S, for each mode can be calculated by Franck-Condon approximation according to eqn (1)-(4) (see Table 4). Vibrational modes with large S values go against the $S_1 \rightarrow S_0$ radiative decay process, thus, small S values are therefore desirable for organic emitters. The results show that (i) the vibrational modes with large S (>0.5) all present in the low-frequency region for all compounds; (ii) NPB possesses the vibrational mode with the largest Huang-Rhys factor (S = 26.901), however, the vibrational modes with the largest Huang-Rhys factors for TPD and mCBP have S = 5.498and S = 11.534, smaller than for NPB; and (iii) the number of vibrational modes with large S for NPB is larger than the numbers for TPD and mCBP, as shown in Table 4, especially in the low-frequency torsional modes (<200 cm⁻¹). We plot the Huang-Rhys factors S versus the normal mode frequencies of the three compounds in Fig. 5. We can see that more vibrational modes are expressed for NPB in the low-frequency region (<1000 cm⁻¹). Calculation results show that the numbers of the strong low-frequency modes of TPD, mCBP, and NPB are 10, 12, and 24, respectively, and all of the modes are torsional modes.³⁴ It shows that the low-frequency modes play an important role in photophysical properties for organic semiconductor materials. Fig. 5 also shows typical vibrational modes for TPD, mCBP and NPB at low-frequency with the highest S

Table 4 Selected parameters of the main strongly elongated internal modes based on optimized geometries

TPD			mCBP			NPB		
$\omega_j^a (\text{cm}^{-1})$	$S_j^{\ b}$	$\lambda_j^c \text{ (cm}^{-1})$	$\omega_j^a (\text{cm}^{-1})$	$S_j^{\ b}$	$\lambda_j^c \text{ (cm}^{-1})$	$\omega_j^a (\text{cm}^{-1})$	$S_j^{\ b}$	$\lambda_j^c \text{ (cm}^{-1})$
						9	26.901	230.6
						13	1.743	22.5
						22	4.725	102.6
						25	6.827	169.4
						31	3.952	124.2
						38	9.305	350.5
			11	11.534	121.3	46	3.467	160.3
23	0.202	4.7	14	2.028	27.5	51	0.864	43.9
31	1.76	54.1	20	0.284	5. 7	56	3.211	180.3
36	3.333	118.8	35	0.2	7	77	1.021	78.9
43	0.335	14.2	53	4.803	253.45	93	0.308	28.8
49	5.498	271.9	55	2.185	120.3	102	0.142	14.5
66	1.072	70.9	57	1.402	79.61	123	0.923	113.3
87	0.155	13.6	81	0.564	45.5	156	0.215	33.3
95	3.564	340.2	87	0.525	45.4	172	0.151	26
426	0.119	50.6	128	0.943	120.8	185	0.247	45.7
780	0.072	56.2	429	0.131	56.1	295	0.067	19.7
			479	0.106	50.9	424	0.066	27.8
						429	0.061	26.4
						486	0.068	33.4
						513	0.059	30.4
						527	0.09	47.7
						535	0.094	50.5
						550	0.073	40.3
						1216	0.115	139.6
1215	0.109	82.6	1211	0.102	123.3	1318	0.065	85.7
1309	0.051	66.4	1313	0.154	202.1	1336	0.118	157.7
1654	0.07	115.3	1660	0.152	252.1	1406	0.326	458.9
1664	0.151	251.6	1668	0.123	205.5	1625	0.058	94.5
						1652	0.074	122.6
						1661	0.122	203.4

^a Vibrational frequencies. ^b Huang-Rhys factors. ^c Reorganization energies.

PCCP

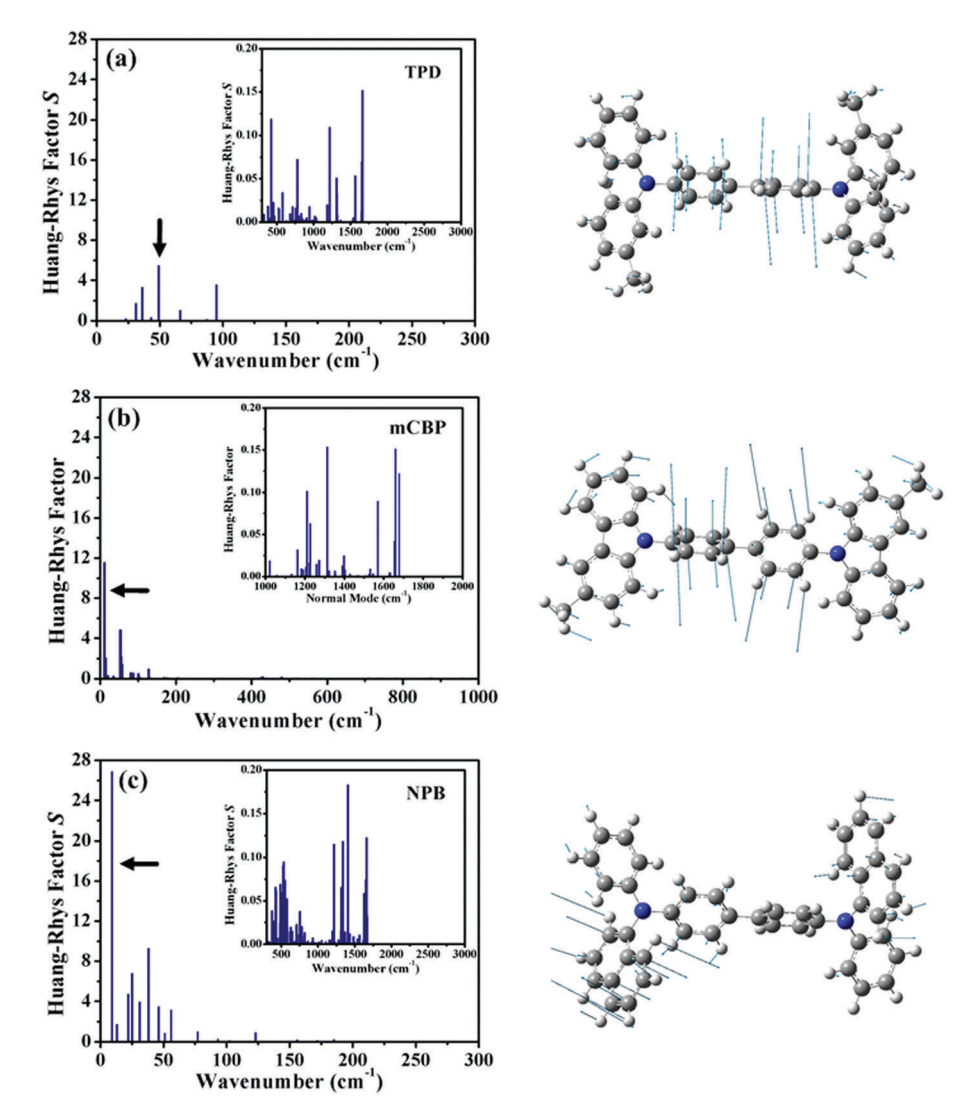


Fig. 5 Calculated Huang-Rhys factors of the normal modes and vibrational modes with the highest S values for TPD, mCBP and NPB.

(indicated by the arrows shown in Fig. 5). We find that the vibrational modes arise from the central biphenyl core for TPD and mCBP, which are out-of-plane torsional modes. However, for NPB, the vibrational modes involve C–C swing vibrations mainly arising from two twisted terminal naphthyl groups, which lead to more low-frequency modes (see Table 4) and will influence the photophysical properties. This reflects the large ρ distribution on the naphthyl moieties as shown in Fig. 3. In addition, for many low-frequency vibrational modes shown in Table 4, the reorganization energy is much larger than the normal mode frequency, which could indicate mode mixing upon electronic excitation. Recently, non-adiabatic molecular dynamics simulations to explore excited-state decay processes are now in progress.

3.5 Radiative and non-radiative decay rates

The calculated radiative decay rates, k_r , at room temperature for TPD, mCBP and NPB are presented in Table 3 based on the equations in Section 2. The calculated results are good agreement with the experimental results in Table 1. We find that the

radiative decay rate for NPB $(0.47 \times 10^8 \text{ s}^{-1})$ is an order of magnitude smaller than the rates for TPD and mCBP (5.53 imes 10^8 s^{-1} and $3.15 \times 10^8 \text{ s}^{-1}$). According to eqn (5) and (6), $k_{\rm r}$ is proportional to μ and N_{FC} . According to the discussion above, the small HOMO-LUMO overlap and the localized distribution of transition density due to naphthyl substituents for NPB result in a small transition dipole moment μ , 35 as evidenced by the transition dipole moment density τ . With regard to $N_{\rm FC}$ considering Huang-Rhys factors S, we evaluate N_{FC} for the three molecules based on Franck-Condon factors (see eqn (2)). The Franck-Condon factor measures the transition probability between a vibrational level of the ground-state and a vibrational level of the excited-state, which is related to the overlap between the wavefunctions of the two vibrational modes in electronic states. Thus, for NPB, the great number of low-frequency torsional modes originating from the peripheral naphthyl groups results

in a small value of the vibration term $\left(\prod_{j} \frac{S_{j}^{n_{j}}}{n_{j}!} e^{-S_{j}}\right)$, which signifies weak vibronic transitions. Consequently, calculated N_{FC}

Paper PCCP

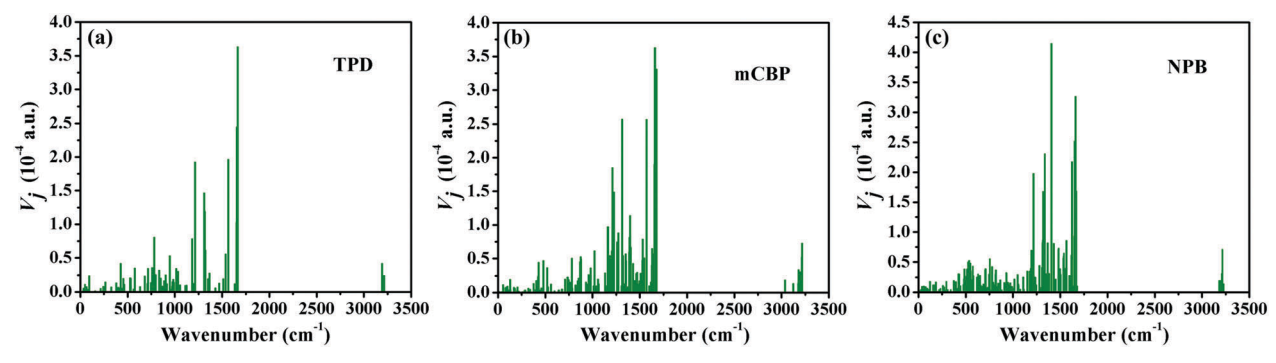


Fig. 6 Vibronic coupling constants for TPD, mCBP and NPB

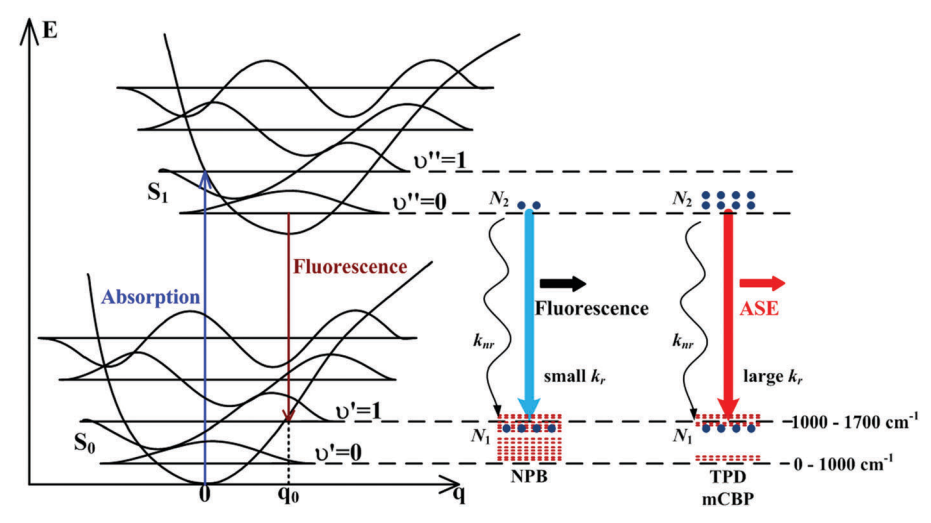


Fig. 7 Schematic for decay processes of TPD, mCBP and NPB

for TPD and mCBP are about 2.5 and 1.6 times larger due to a handful of low-frequency torsional modes than that for NPB. Hence, large μ and $N_{\rm FC}$ lead to an enhanced radiative decay rate $k_{\rm r}$ for TPD and mCBP commonly, where large μ plays a major role.

In addition, we also calculate $k_{\rm nr}$ for the given molecules to investigate the competition between radiative decay processes and non-radiative decay processes. However, k_{nr} is less sensitive to ρ than $k_{\rm r}$ as reported. According to eqn (8) and (9), $k_{\rm nr}$ is proportional to $(V_i)^2$. ³⁰ Fig. 6 shows the calculated values of V_i for TPD, mCBP and NPB. Unlike μ , the V_i values for the three molecules are of the same order. The resulting $k_{\rm nr}$ values for TPD, mCBP and NPB are 5.88 \times $10^{-8}~\text{s}^{-1},\,3.79\times10^{-8}~\text{s}^{-1}$ and $2.64 \times 10^{-8} \, \mathrm{s}^{-1}$, respectively, and are of the same order as well. As we can see, the radiative decay rates k_r for mCBP and NPB are smaller than the rate for TPD. However, $k_{\rm nr}$ of the three compounds are comparable, even after taking into account the vibrational terms. From the calculated values of μ , S_i and V_i , the difference between $k_{\rm r}$ and $k_{\rm nr}$ is larger for NPB than for TPD and mCBP. Comparing k_r values, the radiative decay process is promoted more strongly in TPD and mCBP than in NPB. Then, based on Table 4, calculated total reorganization energy λ in S₁ of TPD, mCBP and NPB is 0.321 eV, 0.379 eV and 0.424 eV, respectively.

The identical λ values offer proof for the same scale $k_{\rm nr}$ of the three molecules.

To evaluate the effect of $k_{\rm r}$ and $k_{\rm nr}$ on ASE performance for organic emitters, then, we analyze the relationship between the ASE threshold and k_r and k_{nr} in accordance with the principle of lasers, as shown in Fig. 7. Due to almost identical values of k_r and $k_{\rm nr}$ for TPD and mCBP, the radiative decay process can compete with the non-radiative decay rate effectively. Inversely, k_r of NPB is one magnitude smaller than $k_{\rm nr}$. According to relation formula $E_{\rm th} \propto 1 + k_{\rm nr}/k_{\rm r}$ and theoretical results of $k_{\rm r}$ and $k_{\rm nr}$, the larger $k_{\rm nr}/k_{\rm r}$ value for NPB compared with TPD and mCBP leads to a large ASE threshold. Thus, large k_r will result in low ASE performance. Moreover, the ASE gain ΔG_{ASE} can be expressed by ΔG_{ASE} = $(N_2 - N_1)Bh\nu/c$, ³⁸ where N_2 and N_1 are the population in the high and low energy level, respectively, B is the Einstein's coefficient, ν is the frequency of light, and c is the velocity of light. Because k_r is proportional to N_2 , large k_r lead to large N_2 , namely large population inversion $N_2 - N_1$. Meanwhile, as we know, Einstein's coefficient B is directly related to k_r : $B \propto (c/8\pi h \nu^3) k_r^{21}$ signifying that $\Delta G_{\rm ASE}$ is proportional to $k_{\rm r}$ as well. Thus, we can infer that large $k_{\rm r}$ is beneficial for the forming of population inversion, generating large ASE gain and a low ASE threshold, and it is a necessary condition for realizing outstanding ASE performance.

PCCP Paper

4 Conclusions

In summary, we cast light on the influence of molecule structure on photophysical properties, and further research the role of the radiative decay rate k_r on the ASE performance of organic emitters. Our calculation results show that enhanced transition densities ρ for TPD and mCBP lead to enhanced transition dipole moments μ . Inversely, the introduction of naphthyl groups with enhanced conjugation for NPB results in spatial separation of the HOMO and LUMO, and the localized distribution of ρ , which generates small μ . Besides, a handful of low-frequency torsional modes make for larger analytical vibrational terms $N_{\rm FC}$ of TPD and mCBP than that of NPB with the prominent structural change between the ground-state and the first excited-state geometries deriving from bulky naphthyl moieties. Therefore, the two aspects together give rise to large k_r , where μ plays a major role. As for the non-radiative decay rate $k_{\rm nr}$, the identical k_{nr} values for the researched molecules promote radiative decay processes in TPD and mCBP, which form effective competition with non-radiative decay processes. Ultimately, large k_r avails remarkable population inversion, large ASE gain and a low ASE threshold. We infer that large k_r is a necessary condition for realizing outstanding ASE performance. In this work, our calculation results provided an explanation for ASE performance in organic semiconductors in view of the radiative decay rate k_r .

Conflicts of interest

There are no conflicts to declare.

Acknowledgements

This work was financially supported by the National Natural Science Foundation of China (Grant No. 61705173), The 111 Project (Grant No. B17035), The Project Supported by Natural Science Basic Research Plan in Shaanxi Province of China (Grant No. 2018JQ6077, 2018JQ6004) and Fundamental Research Funds for the Central Universities (Grant No. JB180504, JBX170513).

References

- 1 S. R. Forrest, Nature, 2004, 428, 911-918.
- 2 G. D. Scholes and G. Rumbles, Nat. Mater., 2006, 5, 683-696.
- 3 B. K. Yap, R. Xia, M. Campoy-Quiles, P. N. Stavrinou and D. D. C. Bradley, Nat. Mater., 2008, 7, 376-380.
- 4 W. Zapka and U. Brackmann, Appl. Phys., 1979, 20, 283-286.
- 5 H. R. Haghighi, S. Forget, S. Chénais, A. Siove and M. Castex, Appl. Phys. Lett., 2009, 95, 033305.
- 6 S. Y. Ma, T. Nakajima and K. Yamashita, Appl. Phys. Lett., 2008, 93, 023306.
- 7 G. Tsiminis, Y. Wang, P. E. Shaw, A. L. Kanibolotsky, I. F. Perepichka, M. D. Dawson, P. J. Skabara and G. A. Turnbull, Appl. Phys. Lett., 2009, 94, 243304.

- 8 N. Tada, S. Tatsuhara, A. Fujii, Y. Ohmori and K. Yoshino, Jpn. J. Appl. Phys., 1997, 36, L421-L424.
- 9 S. Pfeiffer, H.-H. Hörhold, H. Boerner, N. Nikol and W. Busselt, SPIE, 1998, 3476, 258-266.
- 10 R. H. Friend, R. W. Gymer, A. B. Holmes, J. H. Burroughes, R. N. Marks, C. Taliani, D. D. C. Bradley, D. A. D. Santos, J. L. Bredas, M. Logdlund and W. R. Salaneck, Nature, 1999, 397, 121-128.
- 11 S. Gunes, H. Neugebauer and N. S. Sariciftci, Chem. Rev., 2007, 107, 1324-1338.
- 12 J. Zaumseil and H. Sirringhaus, Chem. Rev., 2007, 107, 1296-1323.
- 13 E. M. Calzado, J. M. Villavilla, P. G. Boj, J. A. Quintana and M. A. Díaz-García, Org. Electron., 2006, 7, 319-329.
- 14 D. Schneider, T. Rabe, T. Riedl, T. Dobbertin and O. Werner, Appl. Phys. Lett., 2004, 84, 4693-4695.
- 15 Y. Kawamura, H. Yamamoto, K. Goushi, H. Sasabe and C. Adachi, Appl. Phys. Lett., 2004, 84, 2724-2726.
- 16 T. Aimono, Y. Kawamura, K. Goushi, H. Yamamoto, H. Sasabe and C. Adachi, Appl. Phys. Lett., 2005, 86, 071110.
- 17 H. Nakanotani, N. Matsumoto, H. Uchiuzou, M. Nishiyama, M. Yahiro and C. Adachi, Opt. Mater., 2007, 30, 630-636.
- 18 H. Nakanotani, S. Akiyama, D. Ohnishi, M. Moriwake, M. Yahiro, T. Yoshihara, S. Tobita and C. Adachi, Adv. Funct. Mater., 2007, 17, 2328-2335.
- 19 R. Kabe, H. Nakanotani, T. Sakanoue, M. Yahiro and C. Adachi, Adv. Mater., 2009, 21, 4034-4038.
- 20 T. Komori, H. Nakanotani, T. Yasuda and C. Adachi, J. Mater. Chem. C, 2014, 2, 4918-4921.
- 21 D. H. Kim, A. S. D. Sandanayaka, L. Zhao, D. Pitrat, J. C. Mulatier, T. Matsushima, C. Andraud, J. C. Ribierre and C. Adachi, Appl. Phys. Lett., 2017, 110, 023303.
- 22 Q. Peng, Y. Yi, Z. G. Shuai and J. Shao, J. Am. Chem. Soc., 2007, 129, 9333-9339.
- 23 C. M. Deng, Y. L. Niu, Q. Peng, A. J. Qin, Z. G. Shuai and B. Z. Tang, J. Chem. Phys., 2011, 135, 014304.
- 24 T. Zhang, Y. Q. Jiang, Y. L. Niu, D. Wang, Q. Peng and Z. G. Shuai, J. Phys. Chem. A, 2014, 118, 9094-9104.
- 25 Z. X. Wu, L. Ma, P. Liu, C. H. Zhou, S. Y. Ning, A. El-Shafei, X. Zhao and X. Hou, J. Phys. Chem. A, 2013, 117, 10903-10911.
- 26 L. Ma, Z. X. Wu, T. Lei, Y. Yu, F. Yuan, S. Y. Ning, B. Jiao and X. Hou, Org. Electron., 2014, 15, 3144-3153.
- 27 M. Inoue, T. Matsushima and C. Adachi, Appl. Phys. Lett., 2016, 108, 133302.
- 28 J. L. Brédas, D. Beljonne, V. Coropceanu and J. Cornil, Chem. Rev., 2004, 104, 4971.
- 29 I. Vragovic, R. Scholz and M. Schreiber, Europhys. Lett., 2002, 57, 288-294.
- 30 K. Shizu, H. Noda, H. Tanaka, M. Taneda, M. Uejima, T. Sato, K. Tanaka, H. Kaji and C. Adachi, J. Phys. Chem. C, 2015, 119, 26283-26289.
- 31 S. Manzhos, H. Segawa and K. Yamashita, Chem. Phys. Lett., 2011, 504, 230-235.
- 32 M. Uejima, T. Sato, K. Tanaka and H. Kaji, Chem. Phys., 2014, 430, 47-55.

- 33 Z. L. Cai and J. R. Reimers, *J. Phys. Chem. A*, 2000, **104**, 8389–8408.
- 34 R. Scholz and M. Schreiber, *Chem. Phys.*, 2006, 325, 9–21.
- 35 N. J. Turro, *Modern Molecular Photochemistry*, University Science Books, 1991.
- 36 K. Shizu, M. Uejima, H. Nomura, T. Sato, K. Tanaka, H. Kaji and C. Adachi, *Phys. Rev. Appl.*, 2015, 3, 014001.
- 37 K. Shizu, H. Tanaka, M. Uejima, T. Sato, K. Tanaka, H. Kaji and C. Adachi, *J. Phys. Chem. C*, 2015, **119**, 1291–1297.
- 38 O. Svelto, *Principle of Lasers*, Springer, New York Dordrecht Heidelberg London, 1998.